

ULTRA-SPARSE VIEW RECONSTRUCTION FOR FLASH X-RAY IMAGING USING CONSENSUS EQUILIBRIUM

Maliha Hossain¹, Shane C. Paulson², Hangjie Liao³, Wienong W. Chen², Charles A. Bouman¹

¹School of Electrical and Computer Engineering, Purdue University, West Lafayette, IN, USA,

²School of Aeronautics and Astronautics, Purdue University, West Lafayette, IN, USA,

³Lam Research, 4400 Cushion Pkwy, Fremont, CA 94538, USA

ABSTRACT

A growing number of applications require the reconstruction of 3D objects from a very small number of views. In this research, we consider the problem of reconstructing a 3D object from only 4 Flash X-ray CT views taken during the impact of a Kolsky bar. For such ultra-sparse view datasets, even model-based iterative reconstruction (MBIR) methods produce poor quality results.

In this paper, we present a framework based on a generalization of Plug-and-Play, known as Multi-Agent Consensus Equilibrium (MACE), for incorporating complex and nonlinear prior information into ultra-sparse CT reconstruction. The MACE method allows any number of agents to simultaneously enforce their own prior constraints on the solution. We apply our method on simulated and real data and demonstrate that MACE reduces artifacts, improves reconstructed image quality, and uncovers image features which were otherwise indiscernible.

Index Terms— Sparse View Tomography, In-Situ Tomography, Consensus Equilibrium, Inverse Problems

1. INTRODUCTION

High speed volume visualization of dynamic processes is an emerging application of computed tomography (CT). In particular, Flash X-ray has been used to study explosive and ballistic events [1, 2], material deformation [3], and production line quality control [4], where space and time constraints necessitate sparse view sampling. Even in the absence of such constraints, sparse view CT presents benefits in the form of reduced computation and memory requirements, as well as lower radiation exposure in medical CT.

Conventional CT reconstruction, with a few thousand views, is often performed using analytical reconstruction methods such as Filtered Back Projection (FBP). However, these analytical methods typically generate severe artifacts for sparse view CT problems in which the number of views is subsampled by a factor of 2 to 10. For sparse-view CT, methods such as model based iterative reconstruction (MBIR) must be used to achieve high quality results [5].

When the number of views is less than 10, we enter the domain of ultra sparse CT, and it becomes very challenging to reconstruct high quality CT images. In this case, even established methods such as MBIR tend to generate severe artifacts with reduced contrast and resolution. Recently, Henzler et. al [6] and Shen et. al [7] have independently developed methods for inferring 3D reconstructions from a single medical view using deep learning methods. However, Flash X-ray CT events are typically destructive and stochastic in nature. This makes it difficult to collect the data that would be required to train the machine learning methods. In other recent work, Moser et. al [3, 2] used the algebraic reconstruction technique (ART) to reconstruct 3D volumes from as few as 6 views. However, ART does not allow for the explicit modeling of prior distributions or even the sensor forward model.

Traditional MBIR formulates the reconstruction problem as the solution to a maximum a posteriori (MAP) or regularized maximum likelihood optimization problem [5]. More recently, Plug and Play (PnP) methods [8], originally based on ADMM optimization algorithms [9, 10, 11], have expanded MBIR by allowing the prior distribution to be replaced with advanced denoising operations [12, 13]. Notably, BM3D [14] and its higher dimensional variants are among the best known denoisers that do not require training, and have been found to work particularly well with PnP.

Most recently, Multi-Agent Consensus Equilibrium, or MACE [15] is a generalization of PnP that is based on the solution of a set of equilibrium equations. The MACE equilibrium has the interpretation of being the consensus solution reached by multiple agents each operating in a way that enforces its own preference or constraint. A discussion of practical implementation considerations for fast execution is presented in [16]. Multi-Slice Fusion [17, 18] is a variant of MACE, where multiple lower dimensional denoisers are fused to form a higher dimensional prior model.

In this paper, we introduce a new algorithm, multi-slice fusion with rotational invariance (MSF-RI) for the reconstruction of ultra-sparse tomographic data; and we apply the MSF-RI algorithm to the reconstruction of 4 view CT data from a flash X-ray in-situ imaging system used in a Kolsky bar impact experiment [19]. Our algorithm works by integrating the constraints of four distinct agents using the MACE framework. The first

three agents are based on 2D regularization using BM3D, and the fourth agent enforces partial rotational invariance using a rotational smoothing operator. Our experiments compare MSF-RI to FBP, traditional MBIR, and PnP using a BM4D prior on both synthetic and real data sets. Our proposed MSF-RI method achieves better RMSE and SSIM values than previous methods and reveals structures in our volumetric reconstructions that were previously indistinguishable from streak artifacts.

2. PROBLEM FORMULATION

A CT scan is a collection of X-ray measurements of an object taken at different angles. Reconstructing the object from the scan is an inverse problem with a forward model of the form

$$y = Ax + noise$$

where $y \in \mathbb{R}^M$ is the measurement vector, $A \in \mathbb{R}^{M \times N}$ is the scanner system matrix, and $x \in \mathbb{R}^N$ is the latent image vector we wish to recover. The measurements contain additive Gaussian noise distributed as $N(0, \alpha\Lambda^{-1})$. The MAP cost function then has the form

$$\hat{x}_{MAP} = \arg \min_x \{f(x) + h(x)\} \quad (1)$$

with a forward model term, $f(x) = -\log p(y|x)$, to enforce data fidelity, and a prior model term, $h(x) = -\log p(x)$ to impose regularity. In this case, the forward model term can be written within a constant as

$$f(x) = \frac{1}{2\alpha} \|y - Ax\|_{\Lambda}^2. \quad (2)$$

In practice, it is often difficult to express very complex prior distributions as a single tractable functions $h(x)$. Therefore, the remainder of this section outlines how we will replace this prior with one tailored for our application using MACE.

2.1. MACE framework

Consider the MAP cost function with K regularizers

$$\hat{x}_{MAP} = \arg \min_x \left\{ f(x) + \sum_{k=1}^K \beta_k h_k(x) \right\} \quad (3)$$

where $\beta_k \geq 0$ controls the amount of regularization applied by h_k . The MACE algorithm splits this MAP estimation problem into pieces, with each piece enforced using an agent. For the exact MAP estimation problem, the forward model agent is the proximal map given by

$$F(w) = \arg \min_{z \in \mathbb{R}^N} \left\{ f(z) + \frac{1}{2\sigma^2} \|z - w\|^2 \right\} \quad (4)$$

and the prior model agents are given by

$$H_k(w) = \arg \min_{z \in \mathbb{R}^N} \left\{ h_k(z) + \frac{1}{2\sigma^2} \|z - w\|^2 \right\} \quad (5)$$

where $\sigma > 0$ controls the convergence speed of the algorithm.

Like PnP, MACE allows us to replace the proximal maps H_1, \dots, H_K with more general denoising agents that typically are not proximal maps. Moreover, MACE is a generalization of PnP [15] because it allows for the case of multiple agents, which we will use in this work. Additionally, MACE specifies the solution to the problem using an equilibrium condition, rather than as a solution to an optimization problem. This is important since, in general, the PnP or MACE solution is no longer the solution to a MAP style optimization problem when the agents are not proximal maps.

In order to write the MACE equilibrium condition, define the following notation. Let $\mathbf{w} = [w_0, w_1, \dots, w_K] \in \mathbb{R}^{N \times (K+1)}$ be the concatenation of $K+1$ states where each state will serve as the input to its corresponding agent. Next we define the agent operator,

$$L(\mathbf{w}) = [F(w_0), H_1(w_1), \dots, H_K(w_K)],$$

to denote the parallel application of the $K+1$ agents on their respective state inputs. We also define the averaging operator $G(\mathbf{w}) = [\bar{w}, \dots, \bar{w}]$, where $\bar{w} = \sum_{k=0}^K \mu_k w_k$. The vector $\mu \in \mathbb{R}^{K+1}$ controls the influence each agent exerts on the equilibrium solution and is given by

$$\mu = \frac{1}{1 + \sum_{k=1}^K \beta_k} [1, \beta_1, \dots, \beta_K] \quad (6)$$

Using this framework, the solution to our problem is given by $\hat{x} = \sum_{k=0}^K \mu_k w_k^*$, where w^* is the solution to the consensus equilibrium (CE) equation given by

$$L(\mathbf{w}^*) = G(\mathbf{w}^*). \quad (7)$$

We note that when the agents are the proximal maps of (4) and (5), then $\hat{x} = \hat{x}_{MAP}$ is exactly the MAP estimate of (3).

In [15], it is shown that the CE equations can be solved by using the Douglas-Rachford algorithm to solve for the fixed point of the operator $T = (2G - I)(2F - I)$. Algorithm 1 shows the general method for doing this. When $K = 1$, and $\rho = 0.5$, this algorithm corresponds exactly to PnP implemented with the consensus ADMM algorithm [15], and a sufficient condition for convergence is that T is non-expansive.

Algorithm 1 MACE algorithm

Input: Initial Reconstruction: $x^{(0)} \in \mathbb{R}^N$

Output: Final Reconstruction: x^*

- 1: $\mathbf{w} \leftarrow [x^{(0)}, \dots, x^{(0)}]$
 - 2: **while** not converged **do**
 - 3: $\mathbf{x} \leftarrow L(\mathbf{w})$
 - 4: $\mathbf{z} \leftarrow G(2\mathbf{x} - \mathbf{w})$
 - 5: $\mathbf{w} \leftarrow \mathbf{w} + 2\rho(\mathbf{z} - \mathbf{x})$
 - 6: **end while**
 - 7: **return** $x^* \leftarrow \sum_{k=1}^{K+1} \mu_k x_k$
-

2.2. MACE Agents

Our reconstruction algorithm uses five agents. The first agent, F , enforces data fidelity and is defined in (4) and solved using Iterative Coordinate Descent.

The agents H_1 through H_4 are chosen to enforce spatial regularity and together act as a prior model for reconstruction. More specifically, agents H_1 , H_2 , and H_3 are 2D BM3D denoisers applied to the (\vec{x}, \vec{y}) , (\vec{y}, \vec{z}) , and (\vec{z}, \vec{x}) planes respectively. The H_1 agent independently applies the BM3D denoiser to each (\vec{x}, \vec{y}) slice of the 3D volume. H_2 and H_3 perform similar functions along slices in (\vec{y}, \vec{z}) , and (\vec{z}, \vec{x}) . We refer to this integration of three 2D denoising algorithms as multi-slice fusion (MSF) as described in more detail in [17].

Agent H_4 is designed to enforce weak rotational invariance in the reconstruction. By weak rotational invariance we mean that the reconstructed object should be approximately invariant to small rotations around its axis of symmetry. This is physically reasonable since both the sample under test and the experimental forces are approximately rotationally invariant. Nonetheless, the actual sample will exhibit asymmetric cracks of importance, so H_4 acts to weakly regularize the solution, rather than to enforce strict rotational symmetry.

The weak rotational invariance agent is defined by

$$H_4(x) = \sum_{n=-J}^J \gamma_n R_{n(\theta/J)}(x)$$

where $R_\phi(x)$ rotates the 3D volume, x , around its axis of rotational symmetry by an angle of ϕ . Intuitively, H_4 performs a weighted average of rotations over an angle of 2θ degrees, with weights, γ_j , drawn from a scaled Hamming window.

3. RESULTS

In this section, we present both simulated and real data reconstruction results for a Flash X-ray CT scanner that acquires four views oriented at 18° , 162° , 234° , and 306° [19] using the following five reconstruction algorithms:

Algorithm	Description
FBP	Filtered Back Projection
qGGMRF	MBIR reconstruction is a qGGMRF prior
PnP-BM4D	PnP prior using the 3D denoiser BM4D
MSF	MACE with agents H_1 , H_2 , and H_3
MSF-RI	MACE with agents H_1 , H_2 , H_3 , and H_4

For the simulated cylinder, results and parameters are chosen to minimize RMSE scores achieved using the different priors. For the experimental case, the most visually pleasing results are reported. In all instances of MACE, we set $\rho = 0.4$, and $\theta = 8^\circ$ for H_4 , where applicable. The block matching modules use the implementation in [20] and [21] with default parameters. The PnP and MACE algorithms are all initialized using a qGGMRF reconstruction.

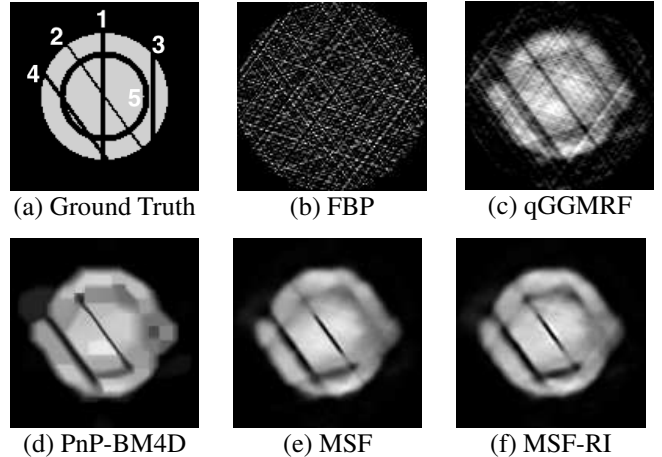


Fig. 1. Simulated results. (a) sample cross section of ground truth for comparison with CT reconstructions (b) through (f) with various methods. (d), (e), and (f) are initialized with the qGGMRF result in (c).

Convergence plots are shown for both datasets in Figures 2 and 5. Distance to convergence is quantified as the RMSE between $G(\mathbf{w})$ and $L(\mathbf{w})$ normalized over \mathbf{w} . This value reflects how closely equation (7) is satisfied. We see that all PnP and MACE algorithms are able to converge to within less than 5% of the final solution.

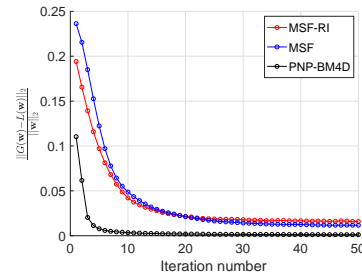


Fig. 2. Convergence rates for phantom reconstruction with PnP-BM4D, MSF, and MSF-RI

3.1. Simulated dataset

Figure 1(a) shows the simulated cylinder phantom with transverse, and radial cracks, typically present in concrete specimens that have been loaded in a Kolsky bar experiment [22]. The volume is 121×121 voxels by 100 slices. Cracks numbered 2 and 4 lie along the view angle at 234° , while 1 and 3 are oriented at 90° . The concentric crack, labelled 5, has been added to further test the model's capabilities. The 3D phantom was forward projected with the parallel beam A matrix and corrupted with AWGN at 20% of the signal strength.

Figures 1(b) through (g) show CT reconstructions of the sample made using the five algorithms, and Table 1 lists the associated normalized root mean squared error (NRMSE) and SSIM values reported for the entire volume.

Notice that FBP fails, and even traditional MBIR performs

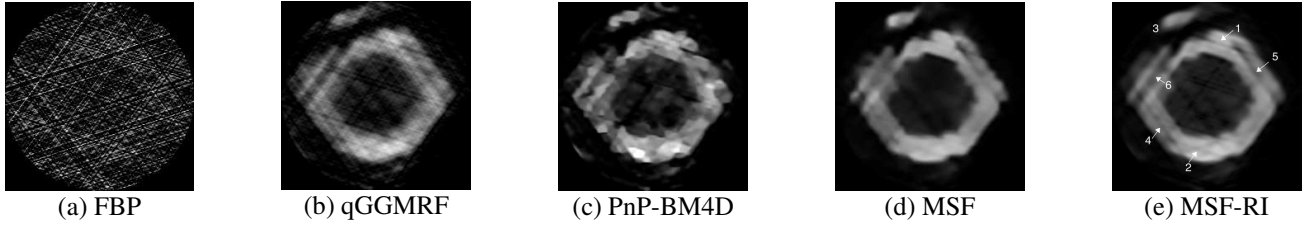


Fig. 3. Reconstructions of slice 21 from experimental dataset. Features of interest are numbered in the result of the proposed method for cross referencing with measurement data.

Table 1. Metrics for simulated dataset reconstruction.

Method	NRMSE	SSIM
FBP	0.8678	0.275052
qGGMRF	0.2389	0.625456
PNP-BM4D	0.2044	0.778083
MSF	0.2006	0.778822
MSF-RI	0.1909	0.789262

poorly on this very underdetermined dataset. PnP-BM4D shows improved results, but generates blocky artifacts. This is likely due to the lack of similar patches in three dimensions as opposed to two dimensions in such a small volume. Consequently, the multi-slice fusion used in MSF is more effective than the BM4D prior, and the result shows more detail. The best result, both visually, and numerically is the MACE-RI algorithm, which reveals the most detail, including the concentric crack 5, and the transverse cracks 2 and 4. Notice that all the methods are effectively blind to crack 1, and crack 3 appears as a blur.

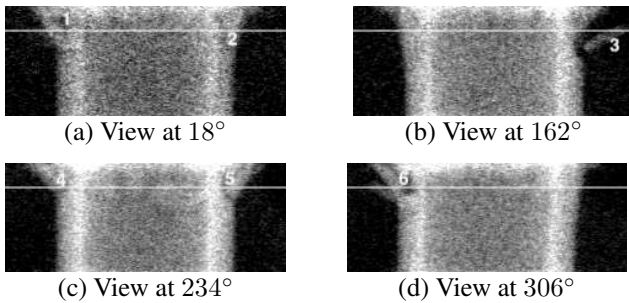


Fig. 4. Experimental view data, where the location of slice 21 is marked with a white line and features of interest are numbered for comparison in reconstructions.

3.2. Experimental dataset

The real sandstone ring dataset is imaged at the moment of impact in the Kolsky bar experiment. The measurement data consists of four views of 478 detector channels per view and 198 slices. After a 2×2 binning factor, the reconstructed volume is 229×229 by 89 slices with voxels of width 0.097 mm. The reconstructions in Figure 3 each depict slice 21 in the (\bar{x}, \bar{y})

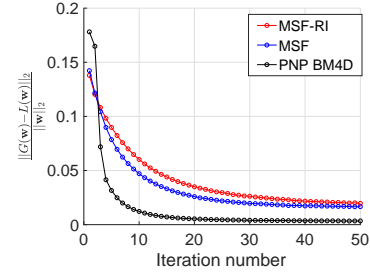


Fig. 5. Convergence rates for reconstruction from of real dataset with PnP-BM4D, MSF, and MSF-RI

plane, which is also marked in the preprocessed view data in Figure 4 by a white line.

Notice that the FBP and qGGMRF results again show severe streaking artifacts that appear along the view angles due to the presence of noise in the projection data. Once again, PnP-BM4D produces blocky regions and cannot resolve the finer cracks. MACE-RI appears to show the most detail with transverse cracks sharpened. The object appears to be delaminating under impact. Cross referencing the cracks with the view data confirms that these cracks are real and not residual streak artifacts.

4. CONCLUSION

In this paper, we demonstrated the versatility of MACE by tailoring an advanced 3D prior model to address the specific needs of the sparse view flash X-ray CT system. We envision a tunable system where end users can combine different agents as modules into the MACE framework to build expressive priors that can exploit geometries of specimens beyond rotational invariance.

5. REFERENCES

- [1] J. Tringe, M. Zellner, C. Mortensen, F. Gagliardi, J. Smith, and K. Champley, “Dynamic three-dimensional observation of corner turning in LX-17 with flash X-rays,” *Bulletin of the American Physical Society*, vol. 64, 2019.
- [2] S. Moser, S. Nau, V. Heusinger, and M. Fiederle, “Investigation of fragment reconstruction accuracy with in situ

- few-view flash X-ray high-speed computed tomography (HSCT),” *Measurement Science and Technology*, vol. 30, no. 6, pp. 065401, 2019.
- [3] S. Moser, S. Nau, M. Salk, and K. Thoma, “In situ flash X-ray high-speed computed tomography for the quantitative analysis of highly dynamic processes,” *Measurement Science and Technology*, vol. 25, no. 2, pp. 025009, 2014.
- [4] M. B. Bauza, J. Tenboer, M. Li, A. Lisovich, J. Zhou, D. Pratt, J. Edwards, H. Zhang, C. Turch, and R. Knebel, “Realization of industry 4.0 with high speed CT in high volume production,” *CIRP Journal of Manufacturing Science and Technology*, vol. 22, pp. 121–125, 2018.
- [5] C. A. Bouman and K. Sauer, “A generalized Gaussian image model for edge-preserving MAP estimation,” *IEEE Transactions on image processing*, vol. 2, no. 3, pp. 296–310, 1993.
- [6] P. Henzler, V. Rasche, T. Ropinski, and T. Ritschel, “Single-image tomography: 3D volumes from 2D cranial X-rays,” in *Computer Graphics Forum*. Wiley Online Library, 2018, vol. 37, pp. 377–388.
- [7] L. Shen, W. Zhao, and L. Xing, “Patient-specific reconstruction of volumetric computed tomography images from a single projection view via deep learning,” *Nature biomedical engineering*, vol. 3, no. 11, pp. 880–888, 2019.
- [8] S. V. Venkatakrishnan, C. A. Bouman, and B. Wohlberg, “Plug-and-play priors for model based reconstruction,” in *2013 IEEE Global Conference on Signal and Information Processing*. IEEE, 2013, pp. 945–948.
- [9] E. Y. Sidky, J. H. Jørgensen, and X. Pan, “Convex optimization problem prototyping for image reconstruction in computed tomography with the Chambolle–Pock algorithm,” *Physics in Medicine & Biology*, vol. 57, no. 10, pp. 3065, 2012.
- [10] S. Ramani and J. A. Fessler, “A splitting-based iterative algorithm for accelerated statistical X]-ray [CT reconstruction,” *IEEE transactions on medical imaging*, vol. 31, no. 3, pp. 677–688, 2011.
- [11] X. Zheng, I. Y. Chun, Z. Li, Y. Long, and J. A. Fessler, “Sparse-view X-ray CT reconstruction using l1 prior with learned transform,” *arXiv preprint arXiv:1711.00905*, 2017.
- [12] T. Balke, S. Majee, G. T. Buzzard, S. Poveromo, P. Howard, M. A. Groeber, J. McClure, and C. A. Bouman, “Separable models for cone-beam MBIR reconstruction,” *Electronic Imaging*, vol. 2018, no. 15, pp. 181–1, 2018.
- [13] S. Sreehari, S. V. Venkatakrishnan, L. F. Drummy, J. P. Simmons, and C. A. Bouman, “Advanced prior modeling for 3D bright field electron tomography,” in *Computational Imaging XIII*. International Society for Optics and Photonics, 2015, vol. 9401, p. 940108.
- [14] K. Dabov, A. Foi, V. Katkovnik, and K. Egiazarian, “Image denoising with block-matching and 3D filtering,” in *Image Processing: Algorithms and Systems, Neural Networks, and Machine Learning*. International Society for Optics and Photonics, 2006, vol. 6064, p. 606414.
- [15] G. T. Buzzard, S. H. Chan, S. Sreehari, and C. A. Bouman, “Plug-and-play unplugged: Optimization-free reconstruction using consensus equilibrium,” *SIAM Journal on Imaging Sciences*, vol. 11, no. 3, pp. 2001–2020, 2018.
- [16] V. Sridhar, X. Wang, G. T. Buzzard, and C. A. Bouman, “Distributed iterative CT reconstruction using multi-agent consensus equilibrium,” *arXiv preprint arXiv:1911.09278*, 2019.
- [17] S. Majee, T. Balke, C. A. J. Kemp, G.T. Buzzard, and C.A. Bouman, “4D X-ray CT reconstruction using multi-slice fusion,” in *2019 IEEE International Conference on Computational Photography (ICCP)*. IEEE, 2019, pp. 1–8.
- [18] S. Majee, T. Balke, C. A. J. Kemp, G. T. Buzzard, and C. A. Bouman, “Multi-slice fusion for sparse-view and limited-angle 4D CT reconstruction,” *arXiv preprint arXiv:2008.01567*, 2020.
- [19] H. Liao, *Flash X-ray tomography of Kolsky bar experiments*, Ph.D. thesis, Dept. Aero. and Astro. Eng., Purdue Univ., West Lafayette, IN, 2018.
- [20] K. Dabov, A. Danieyan, and A. Foi, “BM3D demo software for image/video restoration and enhancement,” 2014, <http://www.cs.tut.fi/foi/GCF-BM3D> (accessed May 27 2019).
- [21] M. Maggioni and A. Foi, “BM4D software for volumetric data denoising and reconstruction,” 2015, <http://www.cs.tut.fi/foi/GCF-BM3D> (accessed May 27 2019).
- [22] S. C. Paulson, M. Hossain, H. Liao, C. A. Bouman, and W. W. Chen, “In-situ flash X-ray tomography of low-strength mortar concrete subjected to low velocity impact,” Submitted for publication, 2020.